PHYSICAL REVIEW APPLIED **15,** 024050 (2021)

Space-Charge Aberrations in Single-Shot Time-Resolved Transmission Electron Microscopy

P. Denham[*] and P. Musumeci
Department of Physics and Astronomy, University of California at Los Angeles, Los Angeles, California 90066, USA

(Received 8 October 2020; accepted 22 January 2021; published 22 February 2021)

In this paper, we discuss effects of space-charge fields on imaging performance in a single-shot time-resolved transmission electron microscope. Using a Green's function perturbation method, we derive analytical estimates for the effects of space-charge nonlinearity on the image formation process and the associated aberration coefficients. The dependence of these coefficients on the initial beam phase space distribution is elucidated. The results are validated by particle tracking simulations and provide fundamental scaling laws for the trade-off between temporal and spatial resolutions in single-shot time-resolved transmission electron microscopy.

DOI: 10.1103/PhysRevApplied.15.024050

I. INTRODUCTION

Transmission electron microscopy (TEM) has proven to be an extremely powerful and versatile tool in all research areas that benefit from imaging at atomic scale spatial resolution [1–3]. Although a tremendous amount of information can be obtained looking at static snapshots of samples with nanometer and subnanometer resolutions, there is a clear potential for breakthrough advances if the reach of the technique could be upgraded to include the study of how the sample structure, composition, and properties change in response to applied stimulus; in other words, with the addition of time as a fourth dimension to electron microscopy [4].

On the other hand, in stark contrast with the exceptional progress in spatial resolution (recently breaking the subangstrom barrier with the introduction of aberration correction [5,6]), the temporal resolution of TEMs is limited due to the intrinsic need of relatively long exposure times to beat the fundamental shot-noise limit of the electron detectors [7]. Given average electron currents in TEM columns (typically much below 1 μA), in order to deliver an illumination dose sufficient to achieve high-quality imaging, time intervals of the order of milliseconds or longer are required.

There have been multiple attempts to address this shortcoming in electron imaging. One solution is to maintain very low currents in the electron column, but synchronize the time of arrival of the electrons at the object plane with the occurrence of the effect being investigated and repeat the specimen illumination millions of time in the same exact manner [4]. This stroboscopic approach has allowed seminal results in the imaging of electric and magnetic field dynamics (PINEM and magnetic vortex) [8,9].

When the sample dynamics cannot be reproduced in the same way continuously (irreversible processes), one has to resort to single-shot illumination, that is, send all the electrons in one bunch whose temporal duration sets the exposure time of the microscope [10–12]. These instruments have been limited to the nanosecond timescale studies, but pushing the resolution to the 10–100 ps range would allow one to study, for example, in material science defect motion and dislocation dynamics and elucidate the role of material heterogeneity in ultrafast phase transitions; in biology, ultrafast high-energy TEMs would allow one to look at cells and viruses in aqueous solutions. Incidentally, single-shot illumination might also be relevant in setups where there are concerns that the electron dose itself would prevent multiple-shot accumulation on the detector [13]. Compared to standard TEM operating modes, the peak current in such single-shot illumination regimes is necessarily many orders of magnitude higher. For example, 10^8 electrons packed in a 10 ps bunch length correspond to peak currents greater than 1 A. At these currents, space-charge effects quickly degrade the quality of the imaging. Recent work has shown that increasing the energy of the electron beam to the megaelectron-volt range allows one to take advantage of relativistic-induced suppression of space-charge forces to restore the microscope spatial resolution [14,15].

Two main kinds of space-charge interactions, smooth mean field effects and binary collisions, have been identified to play a major role in the evolution of the electron

---

[*] pdenham@physics.ucla.edu

beam distribution in a transmission electron microscope. Past studies [14,16,17] focused on numerical investigations to elucidate the effects on the image quality of stochastic binary collisions for prototypical TEM column. On the other hand, computer simulations naturally suffer from a loss of generality as only the behavior in one particular optical setup is quantitatively captured. Analytical formulas and scaling laws would allow one to quickly estimate spatiotemporal resolution limits for microscope setups spanning many orders of magnitude in electron energies and peak currents.

In this paper we build an analytical framework to calculate from first principles the smooth mean field space-charge-induced aberrations, extending previous literature (for a good review, see Ref. [18]) to the relativistic regime and validate our formulas against particle tracking simulations [19] that include both smooth space-charge and stochastic binary effects separately. In particular, we adopt a perturbation method to study the effects of the smooth space-charge field associated with the beam charge density distribution. At first order, the space-charge field simply adds a distributed linear defocusing lens over the entire column. At the next higher order, the space-charge fields give rise to classical aberration coefficients similar to those associated with magnetic lenses, as already recognized in early work by Hawkes and others [20,21]. Some of these nonlinearities simply depend on the initial position on the sample plane and cause a distortion in the final image that could be calibrated in postprocessing. Other terms affect the trajectories regardless of the initial offset, contributing to a blur in the final image plane that amounts to a loss of spatial resolution. One of the main results of this paper is to be able to quantitatively assess these effects and identify the trade-offs between spatial and temporal resolutions for various beam energies. The other important outcome of this study is the identification of possible compensation schemes properly designing the initial beam distribution in the transverse phase space illuminating the sample. In principle, these aberrations can also be corrected by using multipole electron optics in the transport, but the complexity of such systems would quickly become hard to manage as the compensation critically depends on the beam charge distribution.

It is important at this point to note that stochastic Coulomb interaction effects scale like the square root of the charge density in the beam [16], while smooth space-charge effects increase linearly with the beam current. This suggests that, for sufficiently large beam currents (typical for single-shot TEM applications), there is always a regime in which the latter (i.e., the subject of this paper) will be dominating the beam dynamics.

The paper is organized as follows. We first review the Green function approach we use to evaluate analytically the aberrations and benchmark them with particle tracking simulations in a few simple cases where no space charge is present (i.e., for spherical and chromatic aberrations of magnetic round lenses). In this framework, we then move on to the analysis of space-charge-induced nonlinearities in the transport and derive handy analytical expressions for the space-charge aberration coefficients. The formulas obtained do depend on the particular shape of the initial beam phase space, but for simple cases (uniform, Gaussian), they yield practical estimates for the aberrations, enabling quantitative assessment of the trade-offs between spatial and temporal resolutions for various electron column designs. It is envisioned that the results presented in this paper can guide the development and performance expectations of single-shot time-resolved TEM and their scientific application range.

II. LENS ABERRATIONS

The unperturbed radial equation for an electron in a cylindrically symmetric (round) lens field with focusing strength $\kappa(z)$ is given by

$$r'' + \kappa(z) r = 0, \tag{1}$$

where $\kappa(z) = \{B_0(z)/2[B\rho]\}^2$, $B_0(z)$ is the axial lens magnetic field profile, and $B\rho = m_0 c\beta\gamma/e$ is the magnetic rigidity of the beam with m_0 and e the electron rest mass and charge and γ, β the usual relativistic factors. It is well known that the general solution to this equation can be expressed using a symplectic map as

$$\begin{pmatrix} r \\ r' \end{pmatrix} = \begin{pmatrix} C(z) & S(z) \\ C'(z) & S'(z) \end{pmatrix} \begin{pmatrix} r_0 \\ r'_0 \end{pmatrix}, \tag{2}$$

where $C(z)$ and $S(z)$ are two linearly independent solutions to Eq. (1), satisfying $C(0) = 1$, $C'(0) = 0$, $S(0) = 0$, and $S'(0) = 1$. Furthermore, since the mapping is symplectic, $C(z)S'(z) - C'(z)S(z) = 1$. These two solutions are known as cosinelike and sinelike trajectories. Together, they form a basis in the unperturbed trajectory space (i.e., each trajectory can be written as a linear combination of these functions). The corresponding rays are schematically shown in Fig. 1. When $\kappa(z)$ is designed to image over a distance L, $C(L) = M$ and $S(L) = 0$, where M is the magnification. These two conditions ensure that the transport map is imaging because the final position is simply a scalar multiple of the initial position independently of the initial angle.

A. Perturbation of trajectories in a model lens

Throughout the discussion, we allow the space-charge forces whenever present to modify the linear transport, but notably assume that the nonlinearities associated with deviation from design energy, large angles, space charge, etc. induce only small image plane deviations and that the

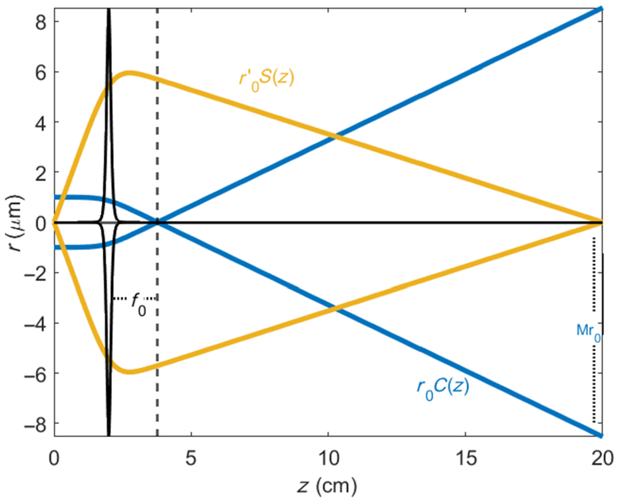

FIG. 1. Schematic example of the two principal trajectories in a thin lens imaging stage.

transport can be well approximated by the first-order linear optics [22]. In order to evaluate the aberrations, we utilize a Green's function approach to solve the driven Hill equation for the electron transverse motion in a TEM column.

In presence of perturbing forces, we then write the particle trajectory as $r = r_c(z) + \delta r(z)$, where $\delta r(z)$ satisfies

$$\delta r'' + \kappa(z)\delta r = f(z) \tag{3}$$

and $r_c(z)$ is the characteristic solution of the Hill equation in the absence of the perturbation $f(z)$.

If we express the driving force as a superposition of impulses, the solution can be written as a convolution integral:

$$\delta r(z) = \int^z G(z,s) f(s) ds. \tag{4}$$

Here the integration interval is from the object to any position along the column up to the image plane and $G(z,s)$ is the Green function of the problem that satisfies

$$\frac{\partial^2 G(z,s)}{\partial z^2} + \kappa(z) G(z,s) = \delta(z-s). \tag{5}$$

Considering separately the cases when $z \neq s$ we can write

$$G(z,s) = \begin{cases} A_1(s)C(z) + A_2(s)S(z), & z < s, \\ B_1(s)C(z) + B_2(s)S(z), & z > s, \end{cases} \tag{6}$$

as a linear combination of the cosinelike and sinelike basis functions.

Applying the proper boundary conditions at $z = s$ [i.e., continuity of G and discontinuity for the derivative as required by integrating once around the δ function in Eq. (5)] we obtain

$$G(z,s) = \begin{cases} C(s)S(z) - S(s)C(z), & z > s, \\ 0, & z < s. \end{cases} \tag{7}$$

This allows us to solve for the excursion from the reference orbits

$$\delta r(z) = \int_0^z [C(s)S(z) - S(s)C(z)] f(s) ds. \tag{8}$$

At the imaging plane, $S(L) = 0$ and $C(L) = -M$, where M is the magnification of the optical system, so the image plane deviations can be written as

$$\delta r(L) = M \int_0^L S(s) f(s) ds. \tag{9}$$

B. Chromatic aberration

The first example of image plane deviation that we analyze is that resulting from the chromatic aberration. A particle with an energy slightly higher (lower) than the design value for the optical column will experience a focusing kick slightly weaker (stronger) than the reference particle. For a small relative momentum deviation $\delta p/p$, the corresponding focusing strength acting on this particle can be approximated by

$$\left(\frac{B_0(z)}{2[B\rho]}\right)^2 \left(\frac{1}{1+\delta p/p}\right)^2 \approx \left(\frac{B_0(z)}{2[B\rho]}\right)^2 \left(1 - 2\frac{\delta p}{p}\right). \tag{10}$$

At first order the equation for the deviation from the reference trajectory can then be written as

$$\delta r'' + \kappa(z)\delta r = 2\frac{\delta p}{p}\left(\frac{B_0(z)}{2[B\rho]}\right)^2 r_c(z), \tag{11}$$

which can be solved using the Green function method described earlier. For sinelike reference trajectories $r_c(z) = r'_0 S(z)$, the image plane deviation is

$$\delta r(L) = M r'_0 \frac{\delta p}{p} \int_0^L \frac{S(s)^2}{2} \left(\frac{B_0(s)}{[B\rho]}\right)^2 ds = M r'_0 \frac{\delta p}{p} C_c, \tag{12}$$

which can be used to evaluate the chromatic aberration coefficient C_c. In Table I we list the nominal optical and beam parameters for the simulation results presented throughout this paper when not indicated differently. In this

TABLE I. Nominal parameters for single solenoid lens stage GPT simulations.

Parameter	Value
Full width pulse length	10 ps
Electron beam kinetic energy	4.3 MeV
Electron beam charge	250 fC
Peak dose at sample	0.5 e/nm^2
Spot size or edge radius	1 μm
Beam divergence	3 mrad
rms energy spread	$< 10^{-5}$
Lens focal length	1.5 cm
Object to image plane distance	20 cm
Magnification	8.5

analysis, the model equation for the on-axis field of the solenoid lens is

$$B_0(z) = \frac{\mu_0}{2}\frac{NI}{d}\left(\frac{z+d/2}{\sqrt{(z+d/2)^2+R^2}} - \frac{z-d/2}{\sqrt{(z-d/2)^2+R^2}}\right) \qquad (13)$$

with physical dimensions of $d = 0.015$ m, $R = 0.008$ m, and N is the number of turns. I is the current which is set to 20 A. The resulting lens has effective length 1.4 cm, and at around 20 A, has a focal length of 1.5 cm for a 4.3 MeV beam. The lens images over a distance of 0.2 m with a magnification of 8.5 times.

In Fig. 2 the chromatic aberration coefficient $C_c = 3$ cm obtained from Eq. (12) is found to be in excellent agreement with the imaging plane deviation obtained from general particle tracer (GPT) [19] simulations performed with space-charge effects turned off for various beam divergence angles as a function of the input energy spread. Note that here and in all the plots that follow in the paper the image plane deviations are divided by the magnification factor to relate them to object plane distances.

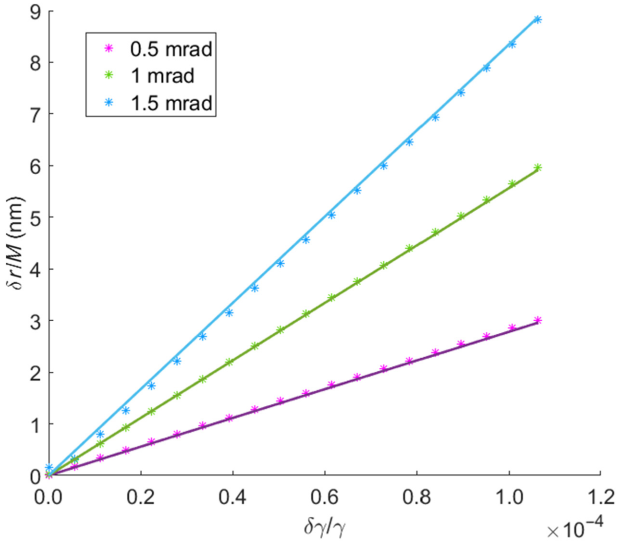

FIG. 2. GPT output of image plane deviations normalized by the magnification and deflection angle and plotted with respect to the rms energy spread.

At vanishing energy spreads, a small difference between the analytical prediction and the simulation results can be noticed and is due to the fact that the imaging is not perfect even in the absence of chromatic aberrations due to the finite beam divergence and the spherical aberration term, which we analyze in the next section.

C. Third-order lens aberrations

Whenever the energy spread of the beam can be kept sufficiently low to minimize the chromatic effects, the main contributions to the trajectory deviation from the ideal imaging condition will be associated with the radial dependence of the focusing field in magnetic round lenses (spherical aberrations). Nonlinear effects arise due to the longitudinal velocity variation through the lens and higher-order terms in the magnetic field components. Following the description in Reiser [23] (and again assuming that these terms can be treated as perturbation), we can write, for the driven Hill equation,

$$\begin{aligned}\delta r'' + \kappa(z)\delta r &= -\kappa(z) r_c'(z)^2 r_c(z) + \kappa(z)\left(\frac{B_0'}{B_0}\right) r_c'(z) r_c(z)^2 \\ &\quad - \left[\kappa(z)^2 - \frac{1}{2}\kappa(z)\left(\frac{B_0''}{B_0}\right)\right] r_c(z)^3 \\ &= f\,[r_c(z), r_c'(z), B_0(z)].\end{aligned}$$

For a general trajectory having initial position and angle offset $r_c(z) = r_0 C(z) + r_0' S(z)$, the deviation at the image plane due to the radial dependence of the lens field can be written as

$$\delta r(L) = M(r_0^3 C_p + 3r_0^2 r_0' C_q + 3r_0 r_0'^2 C_r + r_0'^3 C_s), \qquad (14)$$

where the coefficients with subscripts p, q, r, and s are related to the classical distortion, coma, image curvature, and spherical aberration terms, respectively [20].

The spherical aberration coefficient C_s can be extracted by setting $r_0 = 0$. Then convolution with the Green function at the imaging plane yields

$$\begin{aligned}\delta r(L) &= M r_0'^3 \int_0^L S^4 \left[\kappa\left(\frac{B_0'}{B_0}\right)\left(\frac{S'}{S}\right) + \frac{1}{2}\kappa\left(\frac{B_0''}{B_0}\right) \right. \\ &\qquad \left. - \kappa^2 - \kappa\left(\frac{S'}{S}\right)^2\right] ds \\ &= M r_0'^3 C_s. \end{aligned} \qquad (15)$$

In Fig. 3 we show a comparison for the image plane deviations obtained using the analytical results from Eq. (15) and the numerical GPT simulation for a monochromatic

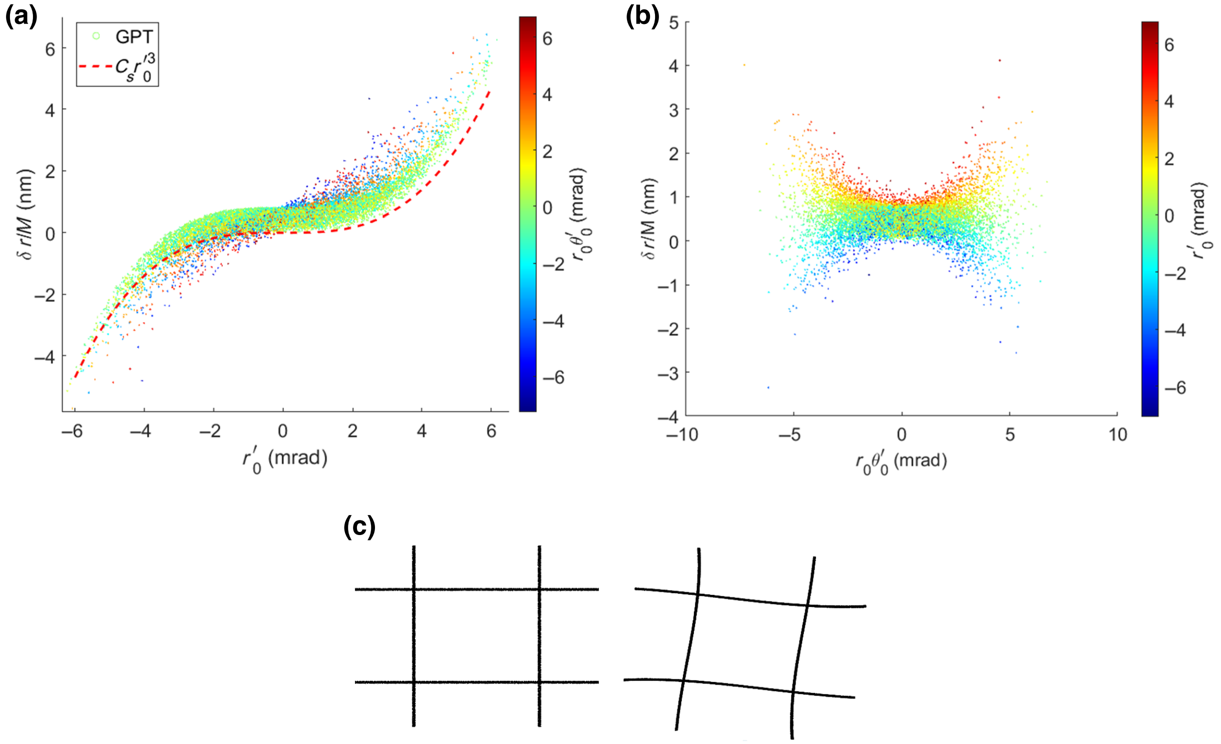

FIG. 3. (a) Image plane deviations from the output of a GPT simulation with no energy spread and no space-charge effects. The dashed line shows the analytical cubic function from Eq. (15). Particles are color coded by initial angular velocity to show the effect of the so-called handkerchief aberration. (b) Image plane output plotted against $r_0\theta'$ after removing spherical aberration cubic dependence. (c) GPT simulation displaying handkerchief distortion of 10 mm hash symbol with 125 μm bar width.

beam with no space charge (and other parameters as listed in Table I). The beam distribution at the object plane is assumed uniform within a 1 μm hard-edge radius and a 3 mrad rms Gaussian angular spread. The excursions from the ideal reference trajectory plotted as a function of the initial ray deflection show excellent agreement between the calculated $C_s = 3$ cm cubic dependence and the particle tracking output. As an example, for incidence angles of 3 mrad, the particular lens employed in our simulation [i.e., Eq. (13)] contributes to a blurring in the image plane of 0.81 nm. Similarly to the chromatic aberration coefficient C_c, it is also typical for C_s to be comparable with the lens focal length. Appropriately crafting the longitudinal on-axis magnetic field profile can reduce the spherical aberration.

The careful reader will notice that, while the cubic dashed line well reproduces the general behavior of the perturbed trajectories, there is an additional broadening of the image deviations obtained from the particle tracking simulation. This is due to another type of lens aberration and deserves a separate discussion. In our simple treatment of the electron dynamics in the cylindrically symmetric column, we neglect the azimuthal motion, but the solenoid Larmor rotation combined with the radial aberrations in Eq. (14) can result in a deviation in the image plane proportional to the square of the particle initial angular velocity $r_0\theta_0'$ [indicated by the color coding in the left figure and more explicitly in Fig. 3(b) that shows the image plane deviation with the cubic spherical aberration subtracted]. We also show the results of a GPT simulation aimed at elucidating this effect (characteristically called the handkerchief aberration) in Fig. 3(c). Here a very large field of view is used so that the handkerchief distortions are clearly visible in the image plane. In general, this effect can be neglected if one is interested in the imaging performances limit at very small transverse offsets from the optical axis.

III. SPACE-CHARGE ABERRATION

In this section, we apply the theoretical framework we developed above to estimate the third-order space-charge-induced deviation from the unperturbed trajectories.

For a very long electron bunch of length L_b (i.e., having a cigar aspect ratio in the beam rest frame), where the input charge density satisfies $(1/\rho)(\partial\rho/\partial z) \ll 1/L_b$, the space-charge field is predominantly two dimensional (2D) and the longitudinal components can be effectively neglected. In this case, for a known charge density distribution and a cylindrically symmetric optical system, the transverse electric field can be derived from a simplified form of Gauss' law:

$$E_r(r;z) = \frac{1}{r}\int_0^r \frac{\rho_{\rm sc}(\xi;z)}{\epsilon_0}\xi\, d\xi. \tag{16}$$

Here ξ is a radial integration variable, and the $z = c\beta t$ dependence in Eq. (16) parameterizes the evolution of the transverse density. Specifically, it represents the average position of the charge distribution in the TEM column. Our strategy for calculating third-order space-charge aberrations proceeds as follows. We start by calculating the transverse charge density evolution using the method of characteristics. Once the evolved transverse density is known, the first- and third-order space-charge fields are computed using Gauss' law. Finally, the third-order field is weighted by Green's function and integrated over the column to obtain deflections of the linear trajectories in the image plane and the corresponding aberration coefficients.

Assuming that the nonlinear space-charge forces only account for a small perturbation on the motion, the particles in the beam will all evolve along characteristic orbits that can be written in the form of a linear transport map $w = Rw_0$, where $w = (x, x', y, y')^\top$ and the 4×4 symplectic matrix R describes the linear uncoupled dynamics in the Larmor frame:

$$R = \begin{bmatrix} C & S & 0 & 0 \\ C' & S' & 0 & 0 \\ 0 & 0 & C & S \\ 0 & 0 & C' & S' \end{bmatrix}. \tag{17}$$

The dynamics are Hamiltonian, so the initial distribution is stationary in phase space. Thus, at any given position along the optical column, the distribution function can be written as $f\,(R^{-1}w) = f\,(w_0)$, where $f\,(w_0)$ is the initial distribution. The space-charge density at any position in the optical column can then be computed by performing the integral over the momentum space, i.e.,

$$\begin{aligned}\rho_{\rm sc}(x,y;z) &= \iint dx'dy' f\,[R^{-1}(x,x',y,y')] \\ &= \iint \frac{du dv}{C(z)^2} f\left(\frac{x - S(z)u}{C(z)}, u, \frac{y - S(z)v}{C(z)}, v\right),\end{aligned} \tag{18}$$

where the substitutions $u = C(z)x' - C'(z)x$ and $v = C(z)y' - C'(z)y$ have been used.

In order to calculate the lowest-order space-charge-induced correction terms in a cylindrical symmetry, we expand the space-charge density in a Maclaurin series as

$$\rho_{\rm sc}(r;z) = \sum_{n=0}^{\infty} \rho^{(2n)}(z)\frac{r^{2n}}{(2n)!}, \tag{19}$$

where the sum only runs through even indices as required by the symmetry and $\rho^{(2n)}$ is the $2n$ radial derivative of the space charge evaluated on the optical axis. The explicitly indicated dependence on z is due to the evolution along the beamline of the $C(z)$ and $S(z)$ transport functions.

Substituting the charge density into Eq. (16), and performing the integral yields

$$E_r(r;z) = \rho^{(0)}(z)\frac{r}{2\epsilon_0} + \rho^{(2)}(z)\frac{r^3}{8\epsilon_0} + \mathcal{O}(r^5), \tag{20}$$

where we truncate the sum after the third-order term.

Similarly to what we did in the previous section, the space-charge aberration can be calculated from the convolution of the nonlinear field evaluated along the reference trajectory with the Green function of the driven Hill equation:

$$\delta r(L) = \frac{eM}{\gamma^3 mc^2\beta^2}\int_0^L \rho^{(2)}(z)\frac{r_c(z)^3}{8\epsilon_0}S(z)dz. \tag{21}$$

Here the relativistic γ^3 term in the denominator takes into account the effects due to the relativistic mass increase and the beam magnetic field forces, and the electron longitudinal velocity $c\beta$ is used to transform the radial acceleration time derivatives into spatial derivatives. Note that the effect of the linear space-charge defocusing field can be included properly, modifying the $C(z)$ and $S(z)$ linear transport trajectories (and adjusting the lens strength to maintain the imaging condition).

Substituting $r_c(z) = r_0C(z) + r_0'S(z)$ yields the space-charge-induced image plane deviation terms similar to Eq. (14), i.e.,

$$\frac{\delta r_{\rm sc}(L)}{M} = r_0^3C_e^{(p)} + 3r_0^2r_0'C_e^{(q)} + 3r_0r_0'^2C_e^{(r)} + r_0'^3C_e^{(s)} \tag{22}$$

with the aberration coefficients explicitly given by

$$C_e^{(p)} = \frac{e}{8\epsilon_0\gamma^3mc^2\beta_0^2}\int_0^L \rho^{(2)}(z)C(z)^3S(z)dz, \tag{23}$$

$$C_e^{(q)} = \frac{e}{8\epsilon_0\gamma^3mc^2\beta_0^2}\int_0^L \rho^{(2)}(z)C(z)^2S(z)^2dz, \tag{24}$$

$$C_e^{(r)} = \frac{e}{8\epsilon_0\gamma^3mc^2\beta_0^2}\int_0^L \rho^{(2)}(z)C(z)S(z)^3dz, \tag{25}$$

$$C_e^{(s)} = \frac{e}{8\epsilon_0\gamma^3mc^2\beta_0^2}\int_0^L \rho^{(2)}(z)S(z)^4dz. \tag{26}$$

A. Space-charge aberrations in the uniform illumination case

We first study the behavior of the aberration coefficients in the particular case in which the sample is uniformly illuminated with a beam having a Gaussian spread in angles.

If the beam is focused to a waist at the specimen location, then the initial phase space distribution can be written as

$$f(x,x',y,y') = \begin{cases} \dfrac{Q}{\pi R_0^2 L_b}\dfrac{1}{2\pi\sigma_\theta^2}\exp\left(-\dfrac{x_0'^2+y_0'^2}{2\sigma_\theta^2}\right), & r_0^2 < R_0^2, \\ 0, & r_0^2 > R_0^2, \end{cases} \tag{27}$$

where Q, R_0, σ_θ, and L_b are the beams total charge, initial edge radius, rms beam divergence in the object plane, and bunch length, respectively.Using the results in the previous section, we can invert the transport map, substitute the initial coordinates in terms of the final coordinates into the distribution function, then integrate over the momentum space to find the charge density evolution along the optical transport. The charge density and its second derivative evaluated on axis are given by

$$\rho^{(0)}(z) = \frac{Q}{\pi\sigma_\theta^2 S^2 L_b}\frac{1-\exp(-p^2/2)}{p^2}, \tag{28}$$

$$\rho^{(2)}(z) = -\frac{Q\exp(-p^2/2)}{2\pi\sigma_\theta^4 S^4 L_b}, \tag{29}$$

where $p = R_0 C(z)/\sigma_\theta S(z)$. Ultimately, the factor p is a proxy that indicates whether or not the transverse spatial distribution has transitioned to being Gaussian or uniform. For large p, the initial spatial distribution dominates and the beam profile is effectively uniform. On the other hand, when p is small, it means that the beam distribution is initial angle dominated and takes a more Gaussian spatial profile, in which case we expect the space-charge field to exhibit a stronger nonlinear character.

We start by noting that in the limit $p \to 0$ (i.e., when $C \to 0$) the expression $[1-\exp(-p^2/2)]/p^2 \to \frac{1}{2}$ and the zero-order density $\rho^{(0)} \to Q/2\pi S^2\sigma_\theta^2 L_b$, i.e, the on-axis density of a Gaussian profile with rms spot size given by $S\sigma_\theta$. Alternatively, when $S \to 0$, such as at a object or image plane, $\rho^{(0)} \to Q/\pi R_0^2 C^2 L_b$, which is the density of a uniformly charged cylinder.

Knowing the second derivative of the space-charge density on axis, we can then use the formulas from the previous section to determine the aberration coefficients

$$C_e^{(p)} = -\frac{K}{8\sigma_\theta R_0^3}\int_0^L p^3\exp(-p^2/2)dz, \tag{30}$$

$$C_e^{(q)} = -\frac{K}{8\sigma_\theta^2 R_0^2}\int_0^L p^2\exp(-p^2/2)dz, \tag{31}$$

$$C_e^{(r)} = -\frac{K}{8\sigma_\theta^3 R_0}\int_0^L p\exp(-p^2/2)dz, \tag{32}$$

$$C_e^{(s)} = -\frac{K}{8\sigma_\theta^4}\int_0^L \exp(-p^2/2)dz, \tag{33}$$

where the perveance factor $K = 2I/I_A\gamma^3\beta^3$, $I = Qc\beta/L_b$ is the beam current, and $I_A \approx 17$ kA is the Alfven current.

For small offsets of the trajectories from the axis, or in other words, if we restrict the field of view to a very small area around the axis, the dominant term in the image plane deviations will be that associated with Eq. (33).

For a setup where $R_0/\sigma_\theta f \ll 1$, the beam spends a majority of the time as a Gaussian, and $\int_0^L \exp(-p^2/2) dz \approx L$. For larger initial spot sizes (or smaller focal waist sizes), the beam will have a Gaussian profile only in a region more localized around the back focal plane of the lens. For the setup corresponding to the electron beam and lens parameters in Table I, the approximation is justified in Fig. 4, where $\exp(-p^2/2)$ is plotted for three different beam divergences. In these cases, we have $I = 25$ mA, $K = 3.6\times10^{-9}$, and $C_e^{(s)} = 1$ m, much larger than any other aberration contribution, so we expect this effect to be dominant at the imaging plane. The sign of the space-charge spherical aberration term is the same as the lens spherical aberrations. Moreover, the linear space-charge forces modify $C(z)$ and $S(z)$, which in turn increases the value of the lens spherical aberration. However, as will be shown, the third-order space-charge effects still dramatically overtake the third-order lens effects by nearly 2 orders of magnitude for a beam current of 25 mA.

Once again we use GPT to validate our model and estimates for $\delta r_{\rm sc}/M$. For this task, we use "spacecharge3Dmesh," the GPT space-charge algorithm that solves Poisson's equation on a mesh in the beam's rest frame [24]. A Lorentz transformation to the comoving frame is then utilized to retrieve the fields that interact with the particles at each time step. The advantage of this approach is that code computation time scales linearly with the number of particles, but the drawback is that the granularity of the particle distribution is not fully taken into account. In a later section at the end the paper we validate these results, comparing the smooth field simulation with the results obtained using "spacecharge3D," a different GPT algorithm that incorporates all Coulomb interactions between the particles.

In Fig. 4(b) we show the transverse electric field felt by the particles at an arbitrary location along the beamline [indicated by the dashed line in Fig. 4(a)] compared with the third-order polynomial calculated from our analytical model. The agreement is excellent and only particles at the head and tail of the beam (where the assumption of an infinite or very long beam breaks down) experience a field deviating significantly from the prediction. The GPT simulation results for the image plane deviations are shown in Fig. 5, in which the overall trend follows the prescribed cubic dependence. For example, using the parameters in

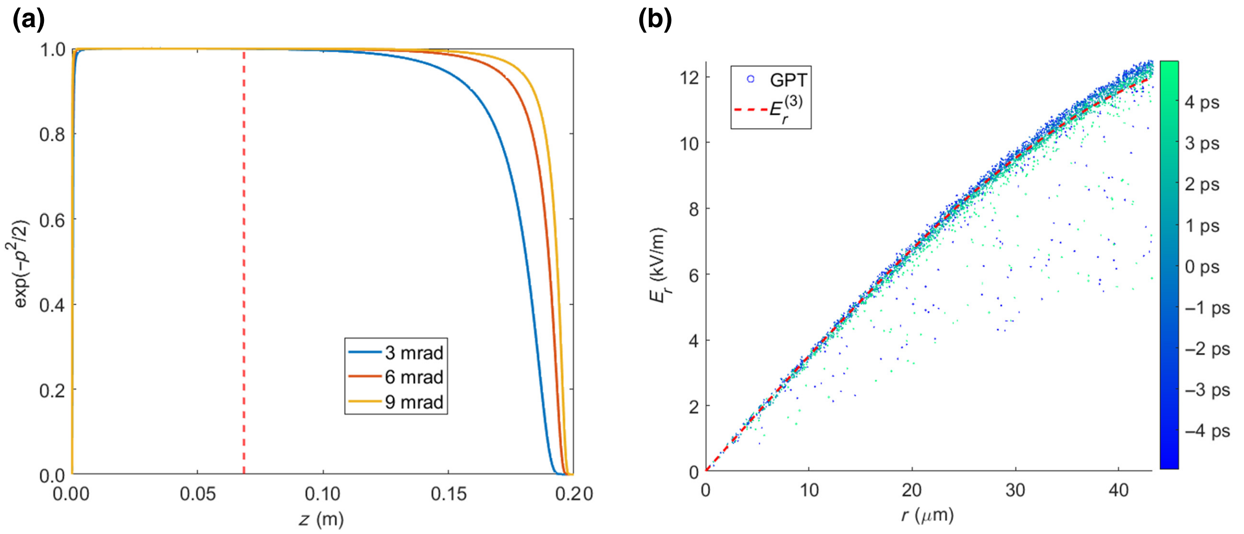

FIG. 4. (a) Nonlinearity coefficient of the charge density distribution plotted from object plane to image plane. At the sampled position along the column indicated by the red vertical dashed line in (a), the radial electric field experienced by each particle as a function of its radial position in the beam is compared with the analytical estimate we use to obtain the space-charge aberration coefficients (b). The particles are color coded with respect to their longitudinal position in the beam.

Table I, for particles incident on the sample with angles of 3 mrad, we expect a 30 nm deviation from the perfect imaging condition. Comparing the y scale with that in Fig. 3 indicates how severe the effect of space-charge-induced aberrations can be on the instrument spatial resolution. The color coding in Fig. 5(a) shows that, even in the space-charge case, handkerchief effects are significant. The magnitude of the handkerchief effect is greatly amplified by the presence of space-charge forces, as can be seen by comparing this figure with Fig. 3(a). This can be easily explained as our analysis is carried out in the Larmor frame and can only predict radial distortions in the image plane. In the laboratory frame the beam rotates due to the solenoid lens field, resulting in handkerchief distortions on the same order as the radial deviations.

The spatial resolution of the instrument can be estimated by the width of the histogram of the image deviations. Before we move forward, it is important to note that, by optimizing the linear defocus of the lens, the width of the projected distribution can be reduced by nearly a factor of 2 with respect to its value at the image plane (see Fig. 6).

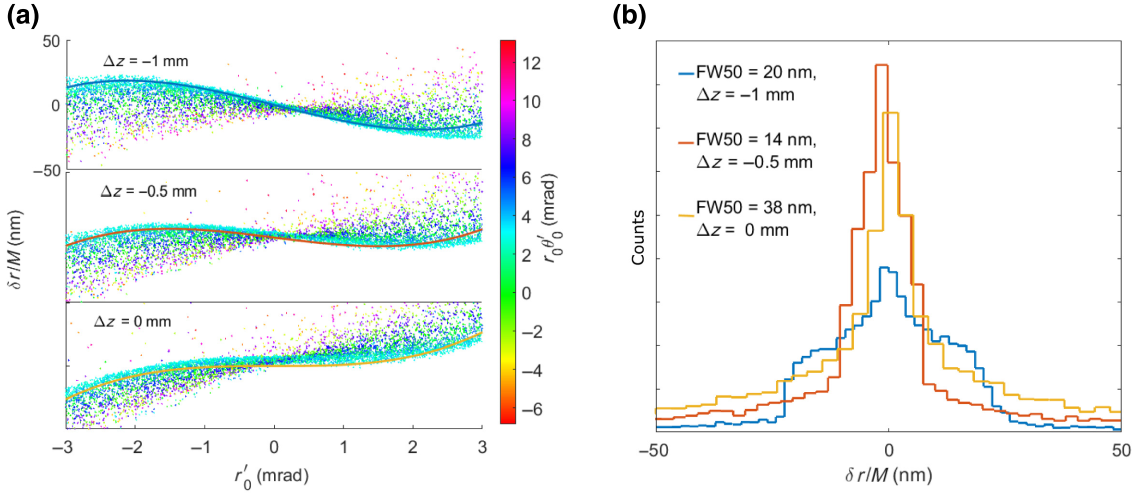

FIG. 5. (a) GPT output of image plane deviations and $\delta r/M = C_e^{(s)} r_0'^3 + \Delta z r_0'/M^2$, with M ≈ 8.5 and $C_e^{(s)} \approx 1$ m, plotted with respect to the initial angle for three different defocus conditions $\Delta z = -1$, -0.5, and 0 mm. The latter corresponds to the linear transport image plane. (b) Corresponding histograms for each defocus position.

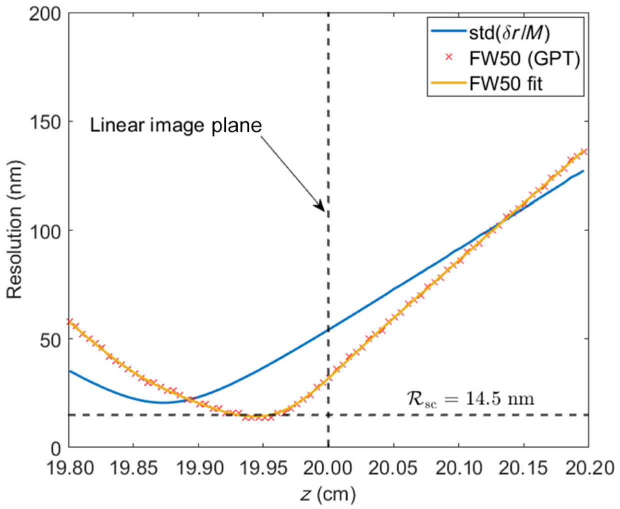

FIG. 6. FW50 and standard deviation of image plane excursions plotted with respect to image plane placement. Linear transport is tuned so that the screen at 20 cm exactly satisfies the imaging condition ($\Delta z = 0$).

This essentially follows from the Scherzer defocus theorem [25]. We can understand what happens more quantitatively by considering the effect on the image plane deviations when moving the output plane back by a small amount Δz. Considering the spherical aberration term, the output plane deviations are given by

$$\delta r = \frac{\Delta z}{M} r'_0 + M C_e^{(s)} r_0'^3. \qquad (34)$$

In the absence of defocus (i.e., $\Delta z = 0$) and assuming a Gaussian angular distribution, the rms spread of the image plane deviations is given by

$$\sqrt{\langle(\delta r/M)^2\rangle} = \sqrt{15} C_e^{(s)} \langle r_0'^2\rangle^{3/2}. \qquad (35)$$

However, it is possible to offset the cubic contribution due to the spherical aberration using a small defocus $\Delta z = -3M^2 C_e^{(s)} \langle r_0'^2\rangle$ for which we have

$$\sqrt{\langle(\delta r/M)^2\rangle_{\rm min}} = \sqrt{6} C_e^{(s)} \langle r_0'^2\rangle^{3/2}, \qquad (36)$$

thus minimizing the rms spread of the image deviations by a factor of $\sqrt{6/15} = 0.6325$.

While rms is the most common quantity to estimate the beam width in accelerator physics, it disproportionately weighs outliers in the distribution. For this reason, in the TEM literature it is common to use the FW50 (full width containing 50% of the beam distribution). The minimum of this quantity in our example is 14 nm, significantly smaller than the rms width at the image plane, as shown in the defocus scan in Fig. 6.

Based on these considerations, in the following section we use an approximation for the instrument spatial resolution of

$$\mathcal{R}_{\rm sc}(I, \gamma, L, \sigma_\theta) \approx \frac{1}{2} C_e^{(s)} \sigma_\theta^3 \cong \frac{KL}{16\sigma_\theta}. \qquad (37)$$

This approximation yields 14.5 nm in our example, which is in close agreement with the GPT simulation. Note that if the lens is sufficiently thin, and the space-charge modified magnification is close enough to the zero-charge magnification, then $L \approx M f_0$, where f_0 is the lens focal length, suggesting that space-charge aberrations would be reduced for smaller focal length optics.

In terms of beam kinetic energy scaling, the perveance is proportional to γ^{-3} and, for a fixed magnetic field profile, the focal length scales as γ^2, so the space-charge contribution to the overall resolution will scale as $IM/\gamma\sigma_\theta$. On the other hand, this assumes that the focal length of the lens can be arbitrarily reduced (i.e., proportional to γ^2), which might not be fully feasible depending on the magnet technology employed.

IV. TRADE-OFFS BETWEEN SPATIAL AND TEMPORAL RESOLUTIONS

With this analytical estimate of the space-charge aberration, it is now possible to estimate the spatial resolution of a time-resolved single-shot transmission electron microscope as a function of the beam energy, beam current, spot size at the sample, and maximum opening angle. The cumulative effect of all competing aberrations caused by spherical, chromatic, space charge, and dose resolution limits is much worse than the diffraction limit $R_d = 1.22(\lambda/\theta)$, where λ is the electron De Broglie wavelength, so we exclude the contribution due to this term in the estimate. Notably, when the beam energy is larger than 700 keV, the electron De Broglie wavelength is less than 1 pm, so a semicollection angle no larger than 5 mrad will have a diffraction limit smaller than a Bohr radius.

Assuming independent contributions, the overall resolution can be estimated by the quadrature sum of all the different sources of excursion from the ideal linear imaging condition along with the resolution limit set by the illumination of the specimen as

$$\mathcal{R} = \sqrt{\left(C_c \frac{\delta\gamma}{\gamma}\sigma_\theta\right)^2 + (C_s\sigma_\theta^3)^2 + \mathcal{R}_{\rm sc}^2 + \frac{\rm SNR^2}{\rm Dose}}, \qquad (38)$$

where SNR = 5 is the desired signal-to-noise ratio set by the Rose criterion, i.e., an experimentally determined standard stating that a signal-to-noise ratio of at least 5 is needed to successfully distinguish features by eye [26], and "Dose" is the particle density at the object plane. This latter term simply indicates that if the electron beam charge is too low, there are just not enough electrons in a resolution pixel to statistically resolve low (20%) contrast features in the image.

The expression for $\mathcal{R}$ in Eq. (38) can be used as a first approximation to the resolution of a single-shot time-resolved TEM. The expression is useful for understand the trade-offs between the different parameters, but does not take into account the correlations between the deviations from the imaging condition (they are not all independent). Detailed numerical simulations would still be required to assess the ultimate resolution limit. In this section we consider Eq. (38) essentially as a multivariate cost function, to be minimized within some reasonable domain of beam and lens parameters to yield the best imaging performances.

For example, the spot size and beam divergence of the beam waist at the sample plane can be optimized using the condenser lens to improve the resolution. Considering the space-charge aberration scaling in Eq. (33), and the inverse dependence on beam divergence makes it clear that increasing beam divergence helps to reduce $\mathcal{R}_{\mathrm{sc}}$ and therefore improve resolution up to the point where spherical aberrations begin to dominate. Similarly, increasing the illumination spot size improves the space-charge resolution, but simultaneously lowers the illumination dose, eventually degrading the imaging performances due to the Rose criterion. An optimal trade-off can be found for given peak current and beam energy. In practice, spot size and divergence at the sample are not independent for a given beam emittance from the electron gun. It is important at this point to note that the contrast mechanism typically used for imaging is to intercept with an aperture the scattered electrons. Therefore, a very large angular divergence at the sample will significantly decrease contrast because the scattered electron distribution gets mixed with the

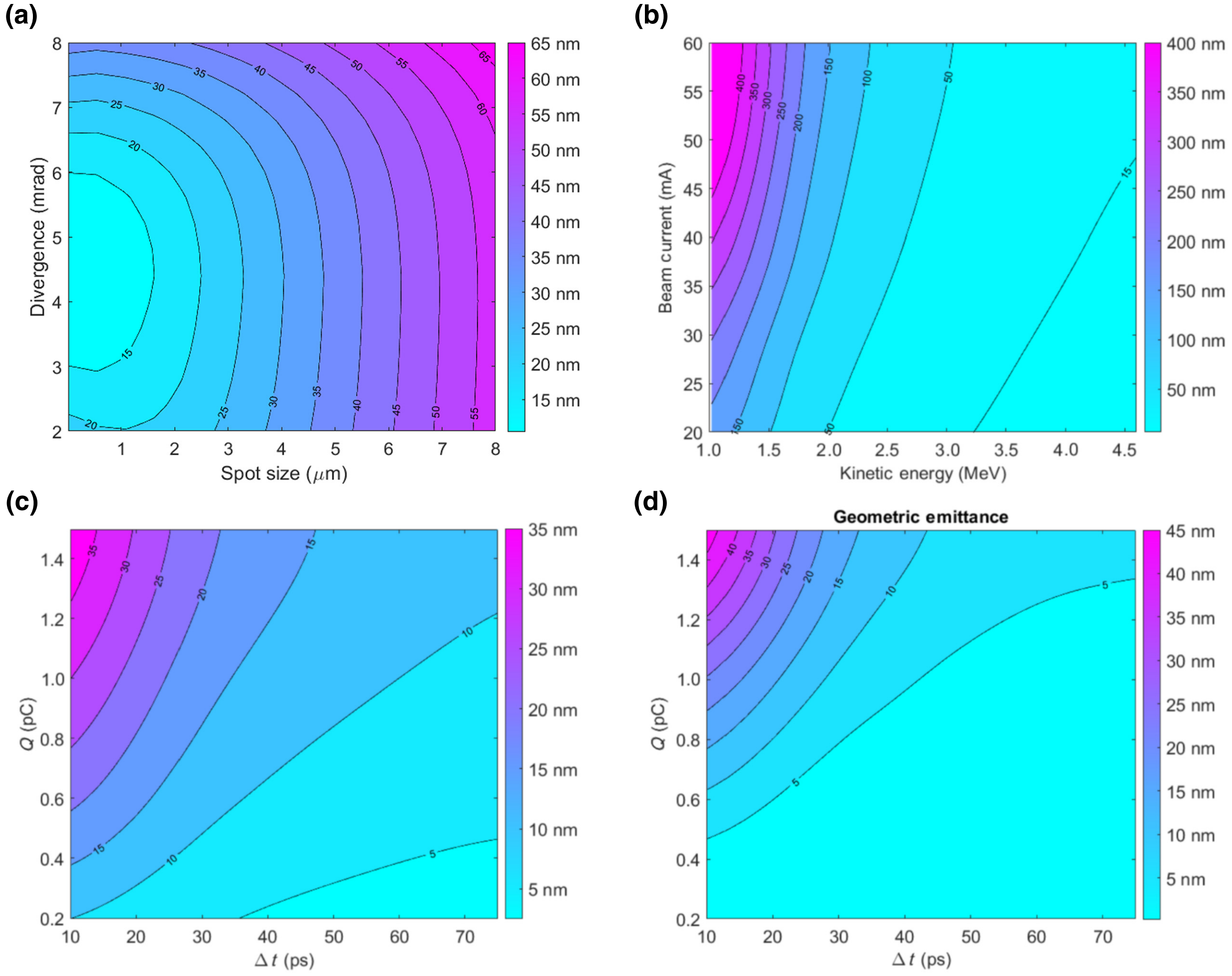

FIG. 7. Analytical and numerical matrix propagator calculations of resolution. (a) Scanned dependence of resolution on illumination geometry for 4.3 MeV kinetic energy and 25 mA peak current. (b) Optimal resolution as a function of beam current and energy. The lens, image, and object plane position are held constant in this plot. For each energy and beam current, the illumination parameters are chosen to optimize the resolution. (c) Optimized resolution for varying beam charge and bunch length for a 4.3 MeV kinetic energy beam. The illumination geometry is optimized at each point and the corresponding required geometric emittance is shown in (d).

transmitted electron distribution, which ultimately causes the object features to become harder to distinguish. A lower beam emittance in this case would provide superior contrast thanks to the lower intrinsic beam divergence.

In Fig. 7(a) we show the estimate for the single-shot TEM resolution plotted for the 4.3 MeV energy and 25 mA peak current as a function of spot size and divergence at the object plane. To generate this plot, the divergence is scanned between 2–8 mrad, and the spot size is varied from 10 nm to 8 μm. The resulting contour map [obtained by plotting Eq. (38)] indicates that nearly 10 nm resolution can be achieved if the beam is focused to 1 μm spot size with $\sigma_\theta = 4$ mrad. GPT simulations are in excellent agreement as analyzing the image plane deviations for this optimized illumination geometry yields a FW50 resolution of 12 nm.

In Fig. 7(b), we show the optimum resolution as a function of beam energy and beam current. This is particularly interesting as there are many different electron sources being considered for ultrafast TEM operation [27–31] and having a rough estimate of the space-charge aberration can be useful to quickly assess potential performances of a proposed TEM. Higher beam energies are clearly favored here, but it should be pointed out that in this plot we kept the focal length constant to a value of 1.5 cm. Note that the magnet technology to obtain such a short focal length becomes more challenging for higher electron energies.

Optimization of the illumination geometry can also be performed for different pulse lengths and charge as long as the beam aspect ratio remains large enough to satisfy the 2D limit approximation. In Fig. 7(c), the illumination geometry is optimized for various bunch lengths and charges. The beam kinetic energy in this plot is kept constant at 4.3 MeV. As expected, lower beam charges and longer pulse lengths both improve the resolution. One aspect to keep in mind is that beam divergence and illuminated area at the sample plane are different (and reoptimized) at each point in the plot, so, for example, a higher beam charge allows one to look at a larger field of view, albeit with lower spatial resolution. This is not surprising as in order to keep the dose above the Rose criterion, the beam must be focused to a smaller spot size, while the aberrations determine the optimal beam divergence. In principle, sub-5-nm resolution can be achieved using bunch lengths longer than 100 ps and emittances smaller than 5 nm.

Finally, in agreement with what was found through numerical simulation in Ref. [14], it is important to note here that additional magnification stages would have much smaller contributions to the smooth space-charge aberrations. Space-charge aberration coefficients in the second stage in our example are up to 10 times larger than those of the first stage. But due to the M times smaller divergence at the entrance to the second stage (hence, M^3 times smaller image disk size scaling) and M times larger "object" size, smooth space-charge effects have a negligible impact on image quality in the second and following stages of the column.

V. MITIGATION EFFECTS. RESHAPING THE DISTRIBUTION

Trading off temporal resolution for spatial resolution may be undesirable for many time-resolved TEM applications. In this section, we investigate the possible resolution improvements that can be attained by exchanging functional dependence of momentum space with real space. In practice, this can be done by using the condenser lens to refocus the beam after an overfilled aperture so that the illuminating momentum distribution is uniform, while the spatial distribution at the sample becomes Gaussian. If the spatial and momentum space configurations are exchanged in this way then the second derivative of the space-charge density modifies to

$$\rho^{(2)}(z) = -\frac{Q\exp\left(-p^{-2}/2\right)}{2\pi\sigma_r^4 C^4 L_b}. \tag{39}$$

In this case, $p = \sigma_r C(z)/\theta_0 S(z)$, where σ_r and θ_0 are the Gaussian rms spot size and hard-edge angular deflection of the object plane distribution. Consequently, the aberration coefficients are also modified to

$$C_e^{(p)} = -\frac{K}{8\sigma_r^3\theta_0}\int_0^L \frac{\exp\left(-p^{-2}/2\right)}{p}dz, \tag{40}$$

$$C_e^{(q)} = -\frac{K}{8\sigma_r^2\theta_0^2}\int_0^L \frac{\exp\left(-p^{-2}/2\right)}{p^2}dz, \tag{41}$$

$$C_e^{(r)} = -\frac{K}{8\sigma_r\theta_0^3}\int_0^L \frac{\exp\left(-p^{-2}/2\right)}{p^3}dz, \tag{42}$$

$$C_e^{(s)} = -\frac{K}{8\theta_0^4}\int_0^L \frac{\exp\left(-p^{-2}/2\right)}{p^4}dz. \tag{43}$$

Ultimately, this particular object plane distribution gives rise to a stronger nonlinear dependence on r_0 and suppressed dependence on r_0'.

This behavior is shown in Fig. 8, where GPT simulation results of the linear image plane are presented. The parameters for this simulations are from Table I, where instead of a Gaussian beam divergence, a uniform angular distribution of up to 3 mrad is used at the object plane. The perveance and peak dose are the same as the beam simulated in Fig. 5. In Fig. 8(a) output image plane deviations are shown color coded with respect to the initial position, r_0. Notably, the particles further from the optic axis,

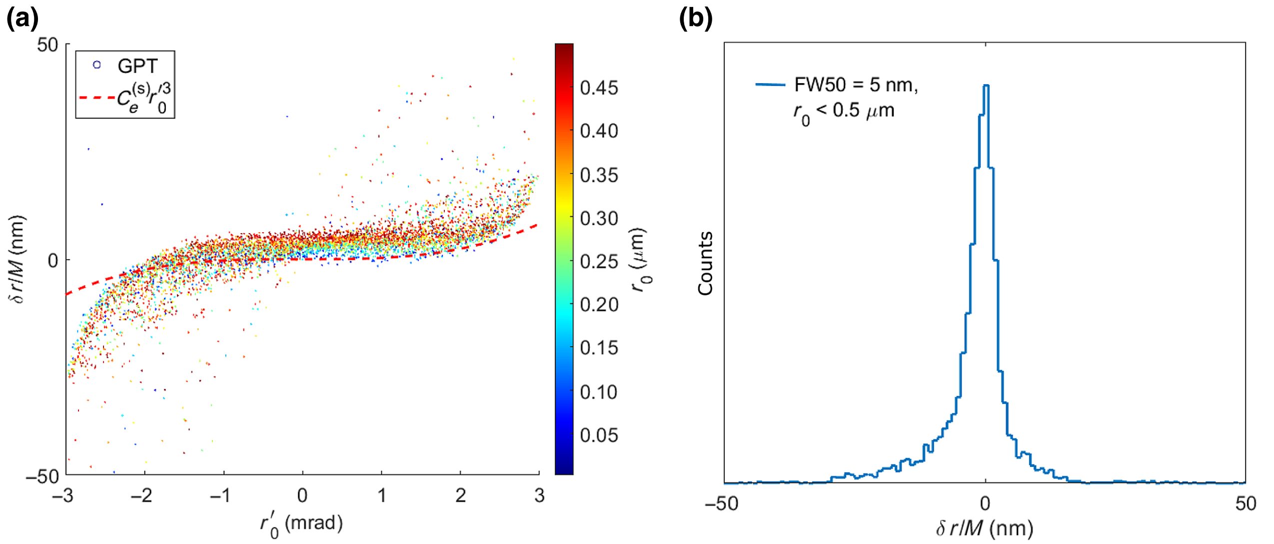

FIG. 8. (a) Image plane deviations as a function of initial angles for the case of a beam with Gaussian spatial illumination and a uniform angular spread. (b) Histogram of the projected distribution within the 0.5 μm object space core.

moving toward the core, have the largest image plane deviation. The sparse residual smearing uncorrelated with r_0 is instead correlated with $r_0\theta_0'$. Plotted along with the output deviations is the predicted spherical aberration curve. The more prominent disagreement from the cubic in Fig. 8 (compared to Fig. 5) is due to the stronger impact of the other space-charge aberration coefficients on this distribution (e.g., $C_e^{(p)}$,$C_e^{(q)}$, and $C_e^{(r)}$). In fact, the theoretical curve well predicts the behavior of $r_0 \rightarrow 0$ particles. However, higher-order contributions in the Taylor series expansion of the charge density are responsible for the residual differences at larger r_0'. In Fig. 8(b), the histogram of the core outputs within a 0.5 μm offset from the optical axis is shown and results in FW50 spatial resolution of 5 nm, nearly a factor of 3 better than the corresponding case of a uniform spatial distribution having a gaussian momentum phase space, indicating that potentially large gains can be obtained by properly shaping the illumination in single-shot time-resolved TEMs.

VI. STOCHASTIC SCATTERING

To provide better context for the analytical estimates discussed in the paper, we perform a final simulation campaign utilizing GPT's “spacecharge3D” algorithm, which takes into account the binary interaction between the particles, with the goal of comparing the image plane deviations obtained with our smooth space-charge model to the general case. Since the computational time in this case scales steeply with the number of particles [$\mathcal{O}(N^2)$], it is convenient to limit the simulation to only a small fraction of the beam. In order to do this, we take advantage of the fact that in the continuous beam approximation (and with very good approximation in the center of flat-top current distributions) the fields do not appreciably depend on the z coordinate, so we can simulate the beam evolution in the column only following a short 100 fs central slice of the entire beam distribution. The reduced number of particles means that the Rose criterion would not be satisfied, but we can assess the spatial resolution considering the FW50 of the image plane deviations. Because of the relativistic dilation of distances in the beam rest frame, aspect ratios still remain very large, and the space-charge field can still be described on average.

The results are shown in Fig. 9, where we compare the FW50 using two different space-charge algorithms in GPT as a function of beam current. The number of particles is

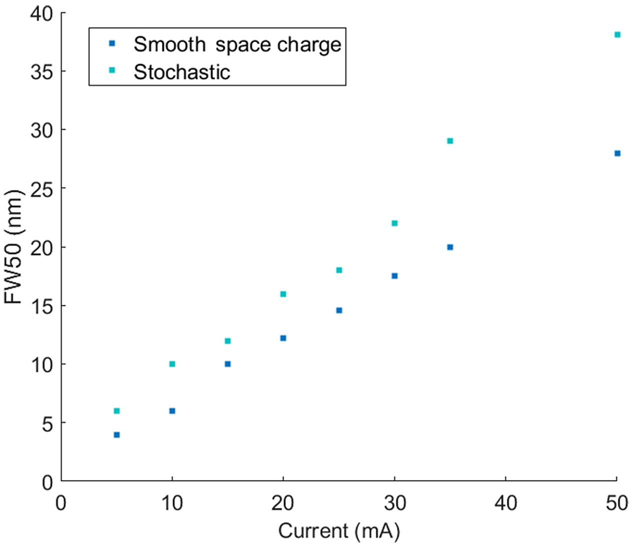

FIG. 9. FW50 comparison between “spacecharge3Dmesh” and “spacecharge3D” models in GPT.

adjusted in each simulation so that each macroparticle represents a single electron. Other than charge, the parameters in Table I are used to generate the beams used in this campaign. Note that the resulting FW50 is dominated by the linear contribution from the smooth space-charge effects. Only a small increase of the FW50 is observed by including binary interactions in the current range simulated. While, for lower beam currents, the binary interaction is proportionally more important and ultimately sets the limit for the spatial resolution, this plot confirms that compensating or correcting for the smooth space-charge effects is a significant challenge in the development of single-shot time-resolved TEMs.

VII. SUMMARY

In summary, taking advantage of the Green function technique to solve the driven Hill equation, we evaluate the smooth space-charge-induced aberrations in a single-shot time-resolved TEM and derive useful analytical expressions that estimate the spatial resolution as a function of relevant beam parameters.

Our analysis is strictly valid in the perturbative regime, that is, when the space-charge nonlinear effects are small compared to the linear forces acting on the beam. Nonetheless, the analysis has been confirmed by benchmarking the results against full particle tracking simulations. The formulas allow quick estimates for the trade-offs between spatial and temporal resolutions in single-shot time-resolved TEMs, as shown in Sec. IV. Ultimately, we show that single nanometer spatial resolution could be achieved using relativistic beam energies, tens of picosecond long bunches, and well-engineered spatial distributions.

In particular, in order to fully reap the benefits associated with the relativistic beam energy, it is important to develop electron optic technology that grants access to very short focal length optical elements in the column. It should also be pointed out that the present discussion only concerns the deviations from the imaging conditions. Other effects come into play when optimizing the energy working point of the instrument. At higher energies, the cross section of interaction for the electrons decreases, so similar specimen thicknesses result in smaller contrast. For the same reasons, higher energy allows thicker samples due to the longer penetration depth. For diffraction contrast, it would be important to balance the tendency of increasing beam divergence to suppress space-charge forces with the requirement of keeping the divergence smaller than the Bragg scattering angles. In addition, electron microscope detectors have been optimized for the 100–300 keV energy range and only very recently direct electron detection for megaelectron-volt electrons has been tested [32].

Finally, more complex optical setups involving quadrupole lenses or even multipole lenses could be employed to further reduce the smooth space-charge aberration effects. The resolution limit of the instrument will then be set by the stochastic blurring associated with information-lossy coulomb collisions between the electrons of the beam in the column after the sample.

We expect this work to elucidate the potential in single-shot time resolved TEMs and guide the developments of future instruments for time-resolved microscopy applications.

ACKNOWLEDGMENTS

A lot of this work is based on D. Cesar's Ph.D. dissertation. We sincerely thank him for the enlightened discussions on the subject and for leading the way in setting up the problem. This work is supported by the DOE STTR Grant No. DE-SC0013115 and by the National Science Foundation under the STROBE Science and Technology Center Grant No. DMR-1548924.

APPENDIX

1. Gaussian space-charge aberration

In the paper we discuss image quality for the cases of illuminating with a uniform beam having a Gaussian angular distribution and a Gaussian beam with uniform angular distribution. Another important case is when the phase space-charge density is a purely Gaussian (both in momentum and position space). For an initially uncoupled beam, we can write

$$\rho = \frac{\lambda \exp[-r^2/2(\sigma_\theta^2 S^2 + \sigma_r^2 C^2)]}{2\pi(\sigma_\theta^2 S^2 + \sigma_r^2 C^2)}. \tag{A1}$$

The on-axis second derivative is found to be

$$\rho^{(2)}(z) = -\frac{\lambda}{2\pi\sigma_\theta^4 S^4 (1+p^2)^2}, \tag{A2}$$

where in this case $p = \sigma_r C(z)/\sigma_\theta S(z)$. The aberration coefficients are then given by

$$C_e^{(p)} = -\frac{K}{8\sigma_r^3\sigma_\theta}\int_0^L \frac{p^3}{(1+p^2)^2}dz, \tag{A3}$$

$$C_e^{(q)} = -\frac{K}{8\sigma_r^2\sigma_\theta^2}\int_0^L \frac{p^2}{(1+p^2)^2}dz, \tag{A4}$$

$$C_e^{(r)} = -\frac{K}{8\sigma_r\sigma_\theta^3}\int_0^L \frac{p}{(1+p^2)^2}dz, \tag{A5}$$

$$C_e^{(s)} = -\frac{K}{8\sigma_\theta^4}\int_0^L \frac{1}{(1+p^2)^2}dz, \tag{A6}$$

where the last term is responsible for the space-charge spherical aberration. The integrand can only be smaller than 1. If $\sigma_r/\sigma_\theta f \ll 1$ (i.e., the spot size is dominated by the initial beam divergence), the integral can be safely approximated to L so that the space-charge spherical aberration of this case is similar to the case of a uniform illumination with a Gaussian angular distribution.

[1] Ludwig Reimer, *Transmission Electron Microscopy: Physics of Image Formation and Microanalysis* (Springer, New York, NY, 2013), Vol. 36.

[2] John C. H. Spence, *High-Resolution Electron Microscopy* (OUP Oxford, Oxford, 2013).

[3] David B. Williams and C. Barry Carter, in *Transmission Electron Microscopy* (Springer, 1996), p. 3.

[4] Ahmed H. Zewail, Four-dimensional electron microscopy, Science **328**, 187 (2010).

[5] Maximilian Haider, Stephan Uhlemann, Eugen Schwan, Harald Rose, Bernd Kabius, and Knut Urban, Electron microscopy image enhanced, Nature **392**, 768 (1998).

[6] Philip E. Batson, Niklas Dellby, and Ondrej L. Krivanek, Sub-ångstrom resolution using aberration corrected electron optics, Nature **418**, 617 (2002).

[7] A. Rose, *Advances in Electronics and Electron Physics* (Academic Press, New York, 1948), p. 131.

[8] Brett Barwick, David J. Flannigan, and Ahmed H. Zewail, Photon-induced near-field electron microscopy, Nature **462**, 902 (2009).

[9] Giovanni Maria Vanacore, Gabriele Berruto, Ivan Madan, Enrico Pomarico, P. Biagioni, R. J. Lamb, D. McGrouther, O. Reinhardt, I. Kaminer, B. Barwick, *et al.*, Ultrafast generation and control of an electron vortex beam via chiral plasmonic near fields, Nat. Mater. **18**, 573 (2019).

[10] H. Dömer and O. Bostanjoglo, High-speed transmission electron microscope, Rev. Sci. Instrum. **74**, 4369 (2003).

[11] Thomas LaGrange, M. R. Armstrong, Ken Boyden, C. G. Brown, G. H. Campbell, J. D. Colvin, W. J. DeHope, A. M. Frank, D. J. Gibson, F. V. Hartemann, *et al.*, Single-shot dynamic transmission electron microscopy, Appl. Phys. Lett. **89**, 044105 (2006).

[12] G. Berruto, I. Madan, Y. Murooka, G. M. Vanacore, E. Pomarico, J. Rajeswari, R. Lamb, P. Huang, A. J. Kruchkov, Y. Togawa, *et al.*, Laser-Induced Skyrmion Writing and Erasing in an Ultrafast Cryo-Lorentz Transmission Electron Microscope, Phys. Rev. Lett. **120**, 117201 (2018).

[13] John C. H. Spence, Outrunning damage: Electrons vs x-rays–timescales and mechanisms, Struct. Dyn. **4**, 044027 (2017).

[14] R. K. Li and P. Musumeci, Single-Shot mev Transmission Electron Microscopy with Picosecond Temporal Resolution, Phys. Rev. Appl. **2**, 024003 (2014).

[15] Chao Lu, Tao Jiang, Shengguang Liu, Rui Wang, Lingrong Zhao, Pengfei Zhu, Yaqi Liu, Jun Xu, Dapeng Yu, Weishi Wan, *et al.*, Imaging nanoscale spatial modulation of a relativistic electron beam with a mev ultrafast electron microscope, Appl. Phys. Lett. **112**, 113102 (2018).

[16] Gerrit H. Jansen, Coulomb interactions in particle beams, Nucl. Instrum. Methods Phys. Res. Sect. A **298**, 496 (1990).

[17] B. W. Reed, M. R. Armstrong, N. D. Browning, G. H. Campbell, J. E. Evans, T. LaGrange, and D. J. Masiel, The evolution of ultrafast electron microscope instrumentation, Microsc. Microanal. **15**, 272 (2009).

[18] Pieter Kruit and Guus H. Jansen, in *Handbook of Charged Particle Optics* (CRC Press, Boca Raton, 1997), Vol. 2.

[19] M. J. De Loos and S. B. Van Der Geer, in *5th European Particle Accelerator Conference* (Institute of Physics Pub., Bristol, 1996), p. 1241.

[20] Peter W. Hawkes and Erwin Kasper, *Principles of Electron Optics* (Academic Press, San Diego, 1996), Vol. 3.

[21] Jon Orloff, in *Encyclopedia of Imaging Science and Technology* (John Wiley & Sons, Inc., Hoboken, NJ, 2002).

[22] Helmut Wiedemann, *Particle Accelerator Physics* (Springer, Berlin, 2007), 3rd ed.

[23] Martin Reiser and Patrick O'Shea, *Theory and Design of Charged Particle Beams* (Wiley Online Library, Weinheim, 1994), Vol. 312.

[24] G. Pöplau, Ursula van Rienen, Bas van der Geer, and Marieke De Loos, Multigrid algorithms for the fast calculation of space-charge effects in accelerator design, IEEE Trans. Magn. **40**, 714 (2004).

[25] O. Scherzer, The theoretical resolution limit of the electron microscope, J. Appl. Phys. **20**, 20 (1949).

[26] Albert Rose, The sensitivity performance of the human eye on an absolute scale∗, J. Opt. Soc. Am. **38**, 196 (1948).

[27] E. Lessner, X. Wang, and P. Musumeci, Report of the basic energy sciences workshop on the future of electron sources, SLAC National Accelerator Laboratory, 2016.

[28] P. Musumeci, J. Giner Navarro, J. B. Rosenzweig, L. Cultrera, I. Bazarov, J. Maxson, S. Karkare, and H. Padmore, Advances in bright electron sources, Nucl. Instrum. Methods Phys. Res. Sect. A **907**, 209 (2018).

[29] J. B. Rosenzweig, A. Cahill, V. Dolgashev, C. Emma, A. Fukasawa, R. Li, C. Limborg, J. Maxson, P. Musumeci, A. Nause, *et al.*, Next generation high brightness electron beams from ultrahigh field cryogenic rf photocathode sources, Phys. Rev. Accelerators Beams **22**, 023403 (2019).

[30] R. Legg, J. J. Bisognano, M. Bissen, R. Bosch, D. Eisert, M. Fisher, M. Green, K. Kleman, J. Kulpin, J. Lawler, *et al.*, in *Proceeding of this Conference, New Orleans, LA* (Joint Accelerator Conferences Website (JACoW), 2012).

[31] Jinfeng Yang, Yoichi Yoshida, and Hiromi Shibata, Femtosecond time-resolved electron microscopy, Electron. Commun. Jpn. **98**, 50 (2015).

[32] Theodore Vecchione, P. Denes, R. K. Jobe, I. J. Johnson, J. M. Joseph, R. K. Li, A. Perazzo, X. Shen, X. J. Wang, S. P. Weathersby, *et al.*, A direct electron detector for time-resolved mev electron microscopy, Rev. Sci. Instrum. **88**, 033702 (2017).